

Cite this: *CrystEngComm*, 2012, **14**, 2756

www.rsc.org/crystengcomm

PAPER

Micro- and nanosized architectures in hydrothermal Tm³⁺-doped GdVO₄: chemical insights towards preservation of the emission efficiency†

Rocío Calderón-Villajos, Carlos Zaldo and Concepción Cascales*

Received 11th November 2011, Accepted 5th January 2012

DOI: 10.1039/c2ce06515k

Chemical processes involving low temperature hydrothermal treatment of pH 4, 7 and 10 solutions of Gd(Tm)-nitrates or chlorides and NH₄VO₃ result in the formation of crystalline nanorods, nanotubes, nanoribbons, nanospindles and 3D micro- or nanoparticles of Tm-doped zircon-type GdVO₄. The relationship between these morphologies and both the structure of the V⁵⁺-precursor in the solution, which depends on the pH, and the hydrothermal treatment has been established. The prepared Tm-GdVO₄ shows excitation (³H₆ → ³H₄) and photoluminescence (³F₄ → ³H₆) spectra of Tm³⁺ involved in the ~1.85 to 2.05 μm laser emission similar to those in single crystals. Room temperature luminescence decays of these excited states exhibit single exponential dynamics for ³F₄ in the lowest Tm³⁺-doped materials, and mostly nonexponential behavior for ³H₄ and ³F₄ in Tm³⁺ concentrated samples, which has been analytically reproduced by the sum of two exponential regimes ascribed to the different rates of nonradiative relaxations in defects at the surface and in the core of the nanocrystals. ³H₄ and ³F₄ fluorescence lifetimes evolve in the sequence $\tau_{pH10} < \tau_{pH4} < \tau_{pH7}$, and highest values $\tau(^3H_4) = 155 \mu s$ and $\tau(^3F_4) = 990 \mu s$ for 0.2 at% Tm³⁺ materials are very close to the radiative lifetimes for Tm³⁺ in the GdVO₄ crystal, $\tau_{RAD} = 174 \mu s$ and $\tau_{RAD} = 1036 \mu s$, respectively.

1. Introduction

Luminescent trivalent lanthanide (Ln)-based oxido nanocrystalline materials exhibit a combination of the classical optical emission properties of the corresponding bulk crystals and original ones derived mainly from surface-related effects.^{1–5} Specifically, while the energy of ^{2S+1}L_J Stark levels remains basically unchanged, and thus the corresponding optical transitions and optical spectra are preserved, luminescence dynamics of Ln in nanocrystals, particularly nonradiative relaxation and energy transfer, can differ from those in bulk materials. These latter differences are directly responsible for observed alteration in emission lifetimes, luminescence quantum yield and concentration quenching, as well as for the new upconversion features described for Ln-doped oxido nanocrystals^{5,6} with regards to bulk counterparts.

The improvement of rapid, high yield and low-cost routes to synthesize Ln-doped nanoparticles supports the current development of derived technological photonic applications, among which the more widely recognized are those related to their use in non-linear fluorescence microscopy as ultrasensitive labels for security⁷ and for cellular imaging,⁸ to the incorporation into

hybrid photonic composites or in the processing of transparent materials to fabricate thin films for IR-excited color displays and generation of bright white light;⁹ as precursors in the manufacture of transparent laser ceramics through dense sintering;¹⁰ or as functional building units in 2D and 3D organized architectures. Among the methods to produce oxido nanoparticles with pure crystal phase and well defined Ln-content, those involving low temperature hydrothermal (HT) treatment of solutions allow an adequate control of their size, dimensionality and even hierarchical organization, through the choice of the experimental conditions during the HT process.^{3–5,11,12}

Tetragonal zircon-type GdVO₄ is a well established laser host possessing relevant characteristics related to the crystal phase stability up to the full Ln replacement of Gd, the broader pumping bandwidth and higher Ln absorption cross-sections than for YAG along with comparable thermal stability,¹³ and their moderate high energy phonons. Its laser emission at ~2 μm is of great interest for a large number of eye-safe related applications and favorable absorption in water, such as in LIDAR systems, materials processing and surgery.^{14,15} In such cases, the laser active cation of choice is Tm³⁺ through its ³F₄ → ³H₆ emission transition at ~1.85 to 2.05 μm. The Tm³⁺ efficient optical absorption at ~800 nm makes possible the pumping with commercially available powerful AlGaAs diode lasers, which supposes a great advantage over traditionally used 2.1 μm Ho³⁺-doped laser crystals. Furthermore, Tm³⁺ electronic transitions are broader than those of Ho³⁺, which favors tunability of the

Instituto de Ciencia de Materiales de Madrid, Consejo Superior de Investigaciones Científicas CSIC, c/ Sor Juana Inés de la Cruz, 3, E-28049 Madrid, Spain. E-mail: ccascales@icmm.csic.es

† Electronic supplementary information (ESI) available. See DOI: 10.1039/c2ce06515k

continuous wave (cw) emission as well as ultrashort (fs) pulsed laser operation.¹⁶ Tm-GdVO₄ materials prepared by hydrothermal synthesis offer a way to the satisfactory development of the earlier indicated specific photonic applications of micro- and nanocrystals.

Here we detail the HT preparation of crystalline Tm-GdVO₄ exhibiting a wide range of morphologies such as nanorods, nanotubes, nanobelts, nanospindles or 3D micro- and nanoparticles. These forms rely on specific synthesis conditions that we have surveyed, mainly the pH of the reaction medium and the time *t* of the HT treatment, as well as the eventual annealing, without using surfactants or external template agents. Previous works have shown that morphologies of HT vanadium pentoxide (V₂O₅), and in general VO_x oxides, are critically dependent on the hydration and protonation degree of V-containing molecular precursors present in the solution medium.¹⁷ In the first part of this work we extend the analysis of the relationship with the structural framework yielded by V-molecular precursors to the morphological characteristics of current hydrothermally prepared Tm-GdVO₄. This survey is carried out to elucidate the chemical formation mechanisms for the latter materials, and thus the influence of preparative conditions to achieve them with suitable size and shape for a given photonic application. The next considered aspect has been to rationalize the impact of size and/or surface features in the technologically interesting Tm³⁺ optical emission at ~1.85 to 2.05 μm through comparison with previous data for single crystals.^{18–22} For the prepared Tm-GdVO₄ the analysis has been carried out through room temperature measurements of both photoluminescence spectra and fluorescence decays of the ³H₄ and ³F₄ Tm³⁺ multiplets, which are involved in the laser emission at this wavelength, for a range of Tm³⁺ concentrations. Since the fluorescence lifetime of ³H₄ and ³F₄ excited states is an intrinsic property of Tm³⁺ in each prepared material, their room temperature measured values will provide a proper insight into the corresponding optical efficiencies with regards to bulk counterparts. This study is usually precluded in nanomaterials by the difficulty associated with spectroscopic measurements in the 2 μm wavelength range, and in fact the scarce data currently available correspond to our previously tested nanorods of Tm-doped Lu₂O₃.^{4,5,23} For this evaluation, Tm-GdVO₄ materials have been classified into three groups following the pH of the HT medium, and furthermore within each group by the HT treatment time *t*. A correlation between ³H₄ and ³F₄ Tm³⁺ measured lifetimes and the size and state of aggregation of primary nanoparticles has been also established.

2. Experimental section

Preparation of samples

Samples (2 mmol) with composition Gd_{1-x}Tm_xVO₄ (*x* = 0.002, 0.005, 0.010 and 0.05, or 0.2, 0.5, 1 and 5 at% Tm) have been synthesized using NH₄VO₃ and lanthanide nitrates (Gd(NO₃)₃·6H₂O, Tm(NO₃)₃·6H₂O, Strem Chemicals 99.99%) or chlorides as reactants. In the latter case Gd(Tm) chlorides were prepared using sesquioxides Gd₂O₃ and Tm₂O₃ (WuXi YiFeng Rare Earth Co Ltd., 99.99%) in the same way as previously described.⁴ The first step involves a sol-gel process, the

preparation of an aqueous solution (distilled water, 40 ml) of the required amounts of the lanthanide source and NH₄VO₃, with the pH adjusted to 4, 7 and 10 by adding dilute NH₄OH under magnetic stirring when needed. Initial dispersions from nitrates had just pH ~4, but in those from chlorides the pH was ~6, and thus dilute HCl was added for adjusting the pH to 4. Orange (pH 4), yellow (pH 7) and white (pH 10) dispersions were maintained under magnetic stirring typically for 1 h, and afterwards were hydrothermally treated at 185 °C for duration times *t* of 2½ h, 6 h, 13 h or 24 h in sealed Teflon-lined autoclaves of 75 ml capacity. The product obtained in each HT reaction was separated by centrifugation, several times washed with distilled water and dried at 120 °C in open air. For lifetime measurements the above samples were further annealed to 600 °C for 5 h. For additional testing of the effect of the synthesis conditions over the morphology some other specific preparations were carried out. These preparations were performed with different conditions for the initial dispersion, either including an aging time without stirring (up to 3 days) or modifying the time of stirring (up to 24 h), incorporating intermediate pH (namely pH 5 and pH 8), as well as with other durations for the HT treatment (*t* from 1 h to 4 days). Further periods of 3 h of immersion in an ultrasound bath, prior or/and after the HT step, were also included in the synthesis procedure of selected Gd_{1-x}Tm_xVO₄ samples.

Characterization of prepared samples

The characterization of the crystalline phase, the shape and size of constituting particles and the vibronic features of prepared Gd_{1-x}Tm_xVO₄ samples have been carried out by 300 K powder X-ray diffraction (XRD, using a Bruker AXS D-8 Advance diffractometer and Cu K_α radiation), field-emission scanning electron microscopy (FE-SEM, with a FEI NOVA SEM230 microscope under accelerating voltages of 5–7 kV), transmission electron microscopy (TEM, using a JEOL 2000FXII microscope with an accelerating voltage of 200 kV), high resolution transmission electron microscopy (HRTEM, using a JEOL JEM3000F operating at 300 kV) and Fourier transform infrared absorption (FT-IR, with a Nicolet 20SXC spectrophotometer in the range 4000–250 cm⁻¹), respectively, in similar ways to that previously described for nanocrystalline Lu₂O₃.⁴ Additionally, hydrodynamic particle size distributions by number, volume and intensity, as well as specific surface, *S*_{BET}, have been measured by dynamic light scattering (DLS, using a Vasco 2-Cordouan equipment with samples dispersed in water), and by adsorption/desorption at 77 K in N₂ atmosphere (with a Micromeritics ASAP 2010 apparatus), respectively.

Tm³⁺ fluorescence was excited at room temperature with a Quanta-Ray MOPO-HF optical parametric oscillator, with the pulse energy at λ = 800 nm of ~32 mJ. The fluorescence was dispersed by a single grating SPEX spectrometer (*f* = 34 cm) and measured with a Hamamatsu InP/InGaAs cooled (-60 °C) photomultiplier, model H9170-75, sensitive in the 950–1700 nm range with a rise time of 0.9 ns or by an InAs Hamamatsu photovoltaic detector cooled to liquid nitrogen and sensitive in the 1500–3100 nm range with a rise time of 0.1 μs. The detector signals were recorded either with a lock-in amplifier for emission and excitation spectra or with a 500 MHz Tektronix oscilloscope,

model TDS-520, for lifetime measurements. A long-wavelength pass filter with cutting edge at 1000 nm was used to remove background excitation light. For these spectroscopic measurements $\text{Gd}_{1-x}\text{Tm}_x\text{VO}_4$ nanoparticles were supported in liquid ethylene glycol, transparent to the infrared fluorescence of Tm^{3+} , $\lambda \approx 1400\text{--}2200$ nm.

3. Results and discussion

Crystal phase, particle size and morphology analyses

A. Influence of preparative conditions on the crystal phase, particle size, size distributions, specific surface and vibronic features of $\text{Gd}_{1-x}\text{Tm}_x\text{VO}_4$ materials. HT syntheses carried out by using Gd(Tm) nitrates or chlorides, at temperature $T = 185$ °C and t from 2½ h to 4 days, at pHs from 4 to 10, have systematically yielded the pure tetragonal $I4_1/amd$ zircon-type phase (JCPDS PDF 86-0996) for all the prepared $\text{Gd}_{1-x}\text{Tm}_x\text{VO}_4$ compositions. However, these preparative conditions, mainly the pH, have a strong influence on the color of the products that varies from orange to yellow and then to pale yellow or white for products prepared from acidic, neutral or highly alkaline dispersions, respectively. Also, the full width at half maximum (FWHM) of observed Bragg peaks in collected XRD patterns depends on the adjusted pH. Fig. 1 shows the XRD patterns of $t = 12$ h HT samples with $\text{Gd}_{0.99}\text{Tm}_{0.01}\text{VO}_4$ nominal composition prepared from nitrates with the initial mixed dispersion at pH 4, 7 and 10. It can be observed the progressive enlargement of the FWHM of Bragg reflections in prepared materials from acidic to highly alkaline syntheses, which corresponds to decreasing mean particle sizes calculated using Scherrer's equation of ~25, 21 and 12 nm, for pH 4, 7 and 10, respectively. XRD patterns after thermal annealing for 5 h at 600 °C show in each case narrower peaks, corresponding to larger calculated mean particle sizes of ~43, 34 and 19 nm for pH 4, 7 and 10, respectively. Fig. S1 in the ESI† compares XRD scans of samples prepared with the same composition $\text{Gd}_{0.995}\text{Tm}_{0.005}\text{VO}_4$ and pH 7, and $t = 2½$ h, 6 h, 13 h and 24 h, using nitrate reagents. They reproduce in all cases

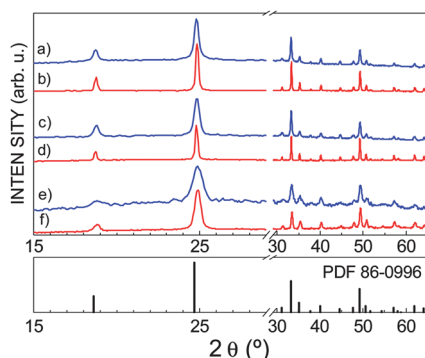


Fig. 1 XRD patterns of $\text{Gd}_{0.99}\text{Tm}_{0.01}\text{VO}_4$ prepared by 12 h of hydrothermal (HT) synthesis at 180 °C using Gd and Tm nitrates and different pHs of the reaction medium: (a and b) acid (pH = 4); (c and d) neutral (pH = 7); (e and f) highly alkaline (pH = 10). Patterns (a), (c) and (e) are for as-prepared samples, and (b), (d) and (f) are for the corresponding materials after annealing at 600 °C for 5 h. For comparison, the XRD pattern scheme of tetragonal $I4_1/amd$ GdVO_4 , JCPDS File 86-0996, is also included.

the scheme of Bragg reflections corresponding to the pure GdVO_4 tetragonal phase, with broader peaks for HT samples prepared from shorter t , with the calculated mean particle size varying from 15 nm ($t = 2½$ h) to 27 nm ($t = 24$ h). Fig. S2† provides the XRD patterns of $\text{Gd}_{0.95}\text{Tm}_{0.05}\text{VO}_4$ samples prepared from Gd(Tm) chlorides at pH 4 and several times of stirring and HT treatment. The comparison of Fig. S2a, b and e† with nitrate counterparts in Fig. S3b and c† and in Fig. 1a indicates larger FWHM for the latter ones. Thus, the preparation of pure $\text{Gd}_{1-x}\text{Tm}_x\text{VO}_4$ with smallest particle size should be favored by specific preparative conditions, namely by using Gd(Tm) nitrate reactants, strong alkaline pH and a short t for the HT treatment, instead of chloride reactants, acidic media and extended HT treatment times. It must be kept in mind that all these earlier indicated XRD calculated sizes would correspond to individual crystalline domains or 'primary crystalline nanoparticles' present in the prepared material.

The HT treatment of acid dispersions of nitrates carried out for very short times ($t = 1$ h) yields orange mixtures of a variable amount of the tetragonal orthovanadate $\text{Gd}_{1-x}\text{Tm}_x\text{VO}_4$ and layered xerogel-like phases, either $\text{V}_2\text{O}_5 \cdot n\text{H}_2\text{O}$,²⁴ see the intense and sharp lines for (00 l) reflections in Fig. S3a†, or NH_4VO_x phases, for instance the sinusoidal layered $\text{NH}_4\text{V}_3\text{O}_8$ compound (monoclinic $P2_1/m$)²⁵ detected in the product of the synthetic process with 1 h of prior magnetic stirring, Fig. S3b†. Although the searched tetragonal phase can be achieved by a 24 h prolonged magnetic stirring in the absence of HT treatment, see Fig. S3c†, it results in a poorly crystallized material.

For a common set of reagents, pH and HT, t , the unit cell parameters calculated by XRD data Rietveld analysis²⁶ progressively decrease for $x = 0.002$ to 0.05 in $\text{Gd}_{1-x}\text{Tm}_x\text{VO}_4$, as expected for the Tm^{3+} replacement of Gd^{3+} . However, depending on the preparative conditions, the presence of a very small variable amount of reduced V^{4+} indicated by the greenish color of the sample prevents further comparisons of unit cell parameters.

Fig. 2a–f show results from DLS measurements on the particle size distribution by number and volume for $\text{Gd}_{0.095}\text{Tm}_{0.005}\text{VO}_4$ samples prepared at pH 4, 7 and 10. For the prepared sample at pH 4, nearly 90% of particles have sizes in the range 150–500 nm, the more abundant fraction with ~300 nm, but they represent only a ~15% of the total volume, since a few particles with larger sizes between 1 and 8 μm constitute the remaining 85% volume, see Fig. 2a and b. For the pH 7-sample, see Fig. 2c and d, ~65% of particles have sizes around 257 nm, and ~20% in the range 320–500 nm, but with ~85% of the total volume constituted by particles of 5 to 8 μm . Particles constituting the pH 10-prepared sample present a narrow size distribution, 99%, having sizes between 23 and 60 nm, one half of them with size just around 23 nm, Fig. 2e and f. Differences between the measured DLS mean particle sizes and those calculated from XRD data, which are considerable for pH 4- and pH 7-samples, arise from the presence in these two latter of a few but large agglomerates of primary nanoparticles, which are bigger for the pH 7 sample. For materials prepared at pH 10 the discrepancy between XRD and DLS calculated average sizes is mainly due to the inclusion of the double layer thickness²⁷ around primary nanoparticles in the aqueous DLS measured dispersion.

Values of the measured specific surface S_{BET} (absorption/desorption) are 6.02/6.45 $\text{m}^2 \text{g}^{-1}$, 20/20 $\text{m}^2 \text{g}^{-1}$ and 32/31 $\text{m}^2 \text{g}^{-1}$

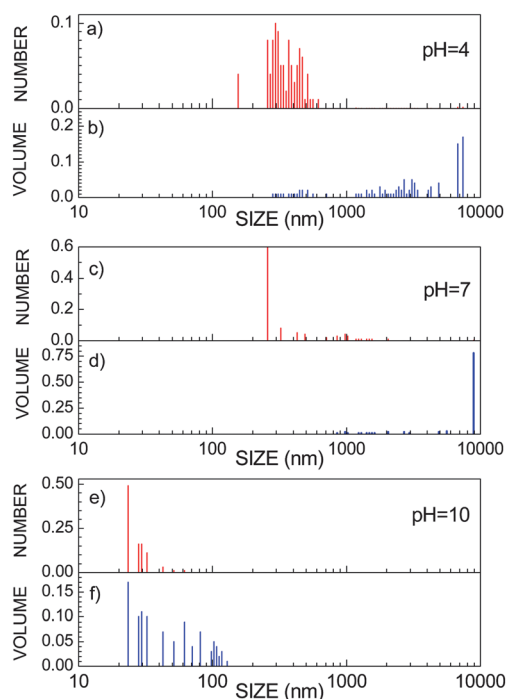


Fig. 2 Distributions by the number and volume of the hydrodynamic size of particles in HT $\text{Gd}_{0.095}\text{Tm}_{0.005}\text{VO}_4$ prepared at different pHs: (a and b) samples at pH = 4; (c and d) samples at pH = 7; (e and f) samples at pH = 10.

for samples with the common composition $\text{Gd}_{0.095}\text{Tm}_{0.005}\text{VO}_4$ prepared at pH 4, 7 and 10, respectively. From S_{BET} data and DLS particle sizes, the estimated average number of primary particles in an aggregate (AAN)²⁷ considerably increase in the order $\text{AAN}_{\text{pH}10} < \text{AAN}_{\text{pH}4} < \text{AAN}_{\text{pH}7}$ -samples, which once again indicates that aggregates are bulkier but constituted by smaller primary crystalline nanoparticles for the pH 7 sample than for the pH 4 one.

Room temperature FT-IR spectra of compositionally equivalent samples from different pHs were also compared to evaluate possible differences. The observed bands are basically the same, as seen in Fig. S4a, b and d† for $\text{Gd}_{0.95}\text{Tm}_{0.05}\text{VO}_4$ materials prepared from nitrate reagents, with peaks at $\sim 450\text{ cm}^{-1}$ and $\sim 820\text{ cm}^{-1}$ assigned to the $\text{Gd}(\text{Tm})\text{O}_8$ and $\nu_3\text{VO}_4^{3-}$ stretching vibrations, respectively, while those centered at $\sim 1630\text{ cm}^{-1}$ and at $\sim 3430\text{ cm}^{-1}$ correspond to HOH bending modes and to OH^- stretching vibrations of lattice water, respectively.²⁸ The sharp peak observed at 1385 cm^{-1} , much more pronounced for the sample from pH = 10, is attributed to the antisymmetric ν_3 mode of surface adsorbed NO_3^- , whose presence is unavoidable when nitrates are used as the lanthanide source in HT syntheses.³ This latter peak as well as the broad bands from lattice water disappear after 5 h of thermal annealing at $600\text{ }^\circ\text{C}$, see Fig. S4c†. Except for the NO_3^- peak, FT-IR spectra of samples prepared with $\text{Gd}(\text{Tm})$ chlorides are the same.

B. Influence of the preparative conditions on the morphology of hydrothermal $\text{Gd}_{1-x}\text{Tm}_x\text{VO}_4$. After a general overview of TEM and SEM images taken for both as-prepared and annealed samples, we perceive that samples prepared in the pH range 4 to

7 consist of particles with mixed morphologies, in some cases with common characteristics at both pHs, while those prepared with pH 10 are single shaped. Furthermore, the use of nitrates or chlorides as the $\text{Gd}(\text{Tm})$ source does not introduce significant differences in the observed forms. Thereafter the description and formation mechanisms will be discussed in the first block for materials prepared at acidic to neutral pH, and afterwards for products yielded with alkaline pH, indistinctively of the lanthanide origin.

Orange to yellow colored $\text{Gd}_{1-x}\text{Tm}_x\text{VO}_4$ HT samples prepared at the pH range from 4 to 7 contain crystalline 3D polygonal nanoparticles (NPs), Fig. 3a and b, and sheets unrolled, Fig. 3c and d, or rolled up at different degrees, Fig. 3e and f, that finally become nanotubes (NTs), Fig. 3g and h. At pH 4 the NPs are getting denser, with better defined form and even larger when the HT reaction time t increases from $t = 2\frac{1}{2}\text{ h}$ to $t = 24\text{ h}$, typically from $\sim 25\text{ nm}$ to $\sim 200\text{ nm}$, see Fig. 3a and b. When the hydrothermal treatment at pH 4 extends for longer periods up to 4 days the coalescence of these NPs generates micrometre sized platelets, which lie parallel to each other, and then self-assemble by stacking with small rotations around a common center, see TEM and SEM images in Fig. 4a–c. The formation of completely closed and flexible $\text{Tm}_x\text{Gd}_{1-x}\text{VO}_4$ NTs having high aspect ratio, some μm long and diameters of ~ 60 to 120 nm , seems to be favored over partially scrolled nanoarchitectures by HT treatments above 13 h at the pH range 4 to 7, see Fig. 3g and h and 5a–c. Assemblies of alongside attached NTs have been also observed under the same synthesis conditions, see Fig. 5d and e. At nearly neutral pH conditions (pH 5 to 7) NPs have a small size of $\sim 25\text{ nm}$, independent of the time of HT treatment, and mainly square or rectangular sections, Fig. 5f and g. Furthermore, nanodots of 3 to 9 nm are surrounding NPs and NTs in samples prepared at pH from 4 to 7, see Fig. 5h and the background images in Fig. 5c and g.

After thermal annealing for 5 h at $600\text{ }^\circ\text{C}$, the morphology of samples prepared within this first pH range and HT treatments up to 24 h experiences some modifications. Fig. 6a shows a typical overview of observed morphologies. 3D NPs appear now rounded and with internal cavities, Fig. 6b, and can coalesce in a highly aligned way, see Fig. 6c and d. Well defined nanorods formed by the ordered assembly of these NPs, Fig. 6e, coexist with highly crystalline nanobelts, either individually, Fig. 7a, or as dense sets of stacked ones, Fig. 7b, which have not been observed in crude HT samples, *i.e.*, nanobelts are specifically generated by the thermal annealing of HT samples.

NTs are also observed, which look rigid and straight, Fig. 7c and d, instead of being flexible as those observed before annealing, and in any case nanorods and especially nanobelts are the predominant 1D morphologies after thermal annealing of HT samples prepared in acidic and nearly neutral pH medium. Some dense micrometre-sized ($1\text{--}8\text{ }\mu\text{m}$) particles have been also seen, in agreement with previous DLS analyses, see Fig. 7e showing large octahedral-like particles, which appear agglomerated and in some cases encircled by nanobelts. Forms in Fig. 7 can be festooned with discrete small polygonal NPs. On the other hand, samples prepared for a prolonged period, 3–4 days, of HT treatment do not undergo noticeable changes upon thermal annealing, that is, they are constituted by dense micrometre sized platelets.

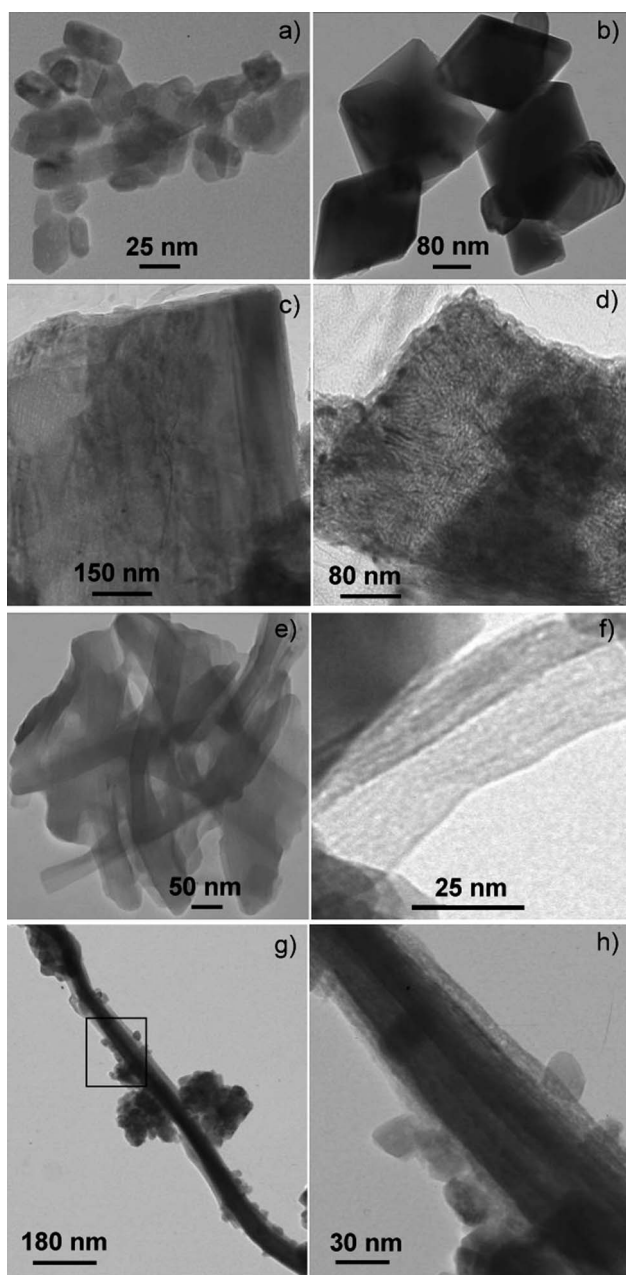


Fig. 3 TEM images of the mixed morphologies of $Gd_{1-x}Tm_xVO_4$ prepared by HT synthesis at pH 4: (a) 3D nanoparticles after $t = 6$ h; (b) dense 3D nanoparticles after $t = 24$ h; (c and d) sheets; (e and f) scrolled forms; (g and h) flexible nanotubes, from $t = 2\frac{1}{2}$ h to 24 h. For the latter the preparation included a further 3 h ultrasonication treatment.

HT syntheses of $Gd_{1-x}Tm_xVO_4$ carried out in the alkaline pH range of 8 to 10 produce pale-yellow to colorless NPs with spindle-like to round-shaped grain morphologies. The nanospindles appear at the lower side of this pH range, and seem to be formed by ribbon-like particles ~ 10 nm of diameter alongside aligned, with a full length of 70–100 nm, see Fig. 8a and b. Spindles are in all cases highly porous, and show a slightly higher aspect ratio when prepared from chlorides than from nitrates, compare images in Fig. 8a and b with those in Fig. 8c and d, for chloride and nitrate reagents, respectively. A nearly

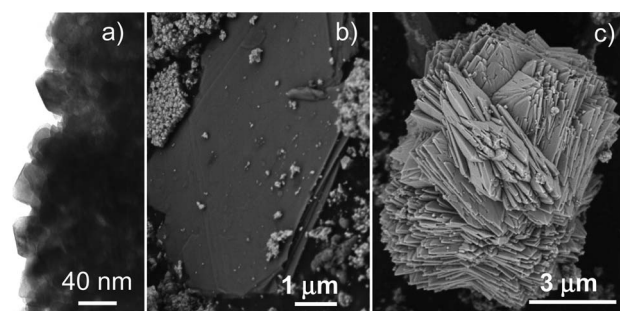


Fig. 4 $Gd_{1-x}Tm_xVO_4$ prepared by prolonged HT treatment at pH 4: (a) TEM image of coalescent nanoparticles after 2 days; (b and c) FE-SEM images of stacked platelets after 3 days.

homogeneous size distribution of nanospindles is obtained for usual preparations with no aging time and then hydrothermally treated for $t = 2\frac{1}{2}$ to 24 h. By prolonging both the aging time of the dispersion and its subsequent HT treatment the spindles become larger, with ~ 40 nm wide and 230 nm long, and their previously observed frontiers between individual nanoribbons disappear, and further round-shaped NPs of ~ 20 nm are also present, see Fig. 8e. Higher pH and to some extent the annealing produce NPs with round-shaped grain morphology and homogeneous size distribution, see Fig. 8f.

C. Growth mechanisms: relationship with VO_x crystalline phases resulting from V^{5+} molecular precursor species in the starting dispersion. For previously reported sol-gel,²⁹ ultrasonicated-driven^{30,31} or HT^{32–39} synthesized tetragonal $REVO_4$ NPs, apart from the description of the shape and the envisaged formation process in each particular case, a comprehensive discussion of the chemical origin of their observed morphologies remains still lacking. Recently, clear correlations have been established between the observed morphology of micro- and nanosized HT vanadium oxides (VO_x) and the structure of molecular V^{5+} -precursors present in the starting sol-gel dispersion.¹⁷

The most important parameter governing the availability of specific molecular precursors is the pH of the dispersion, and to some extent the temperature, although the presence of foreign anionic species can also play a role in self-assembling routes of such precursors.¹⁷ At this point we must consider the close resemblance of the above described $Gd_{1-x}Tm_xVO_4$ shapes with those observed for nanostructured VO_x prepared by HT treatment of dispersions containing V^{5+} over a wide pH range.¹⁷ Thus we think that the molecular V^{5+} -precursor eventually present in particular synthesis conditions, which provides a VO_x -specific crystalline structure, is also the common factor to be considered for the general understanding of the origin of current $Gd_{1-x}Tm_xVO_4$ nanostructures. Moreover, the deep significance of the observed strong differences in color of $Gd_{1-x}Tm_xVO_4$ NPs depending on the pH of the starting dispersion, just as in the system of HT VO_x , was the initial support of the confidence on results from this analysis.

Dense 3D polygonal forms as those shown in Fig. 3a and b, observed for HT preparations at low pH, are related to the presence in the initial dispersion of anionic decavanadate clusters, $[V_{10}O_{28}]^{6-}$. The formation of these latter anionic entities,

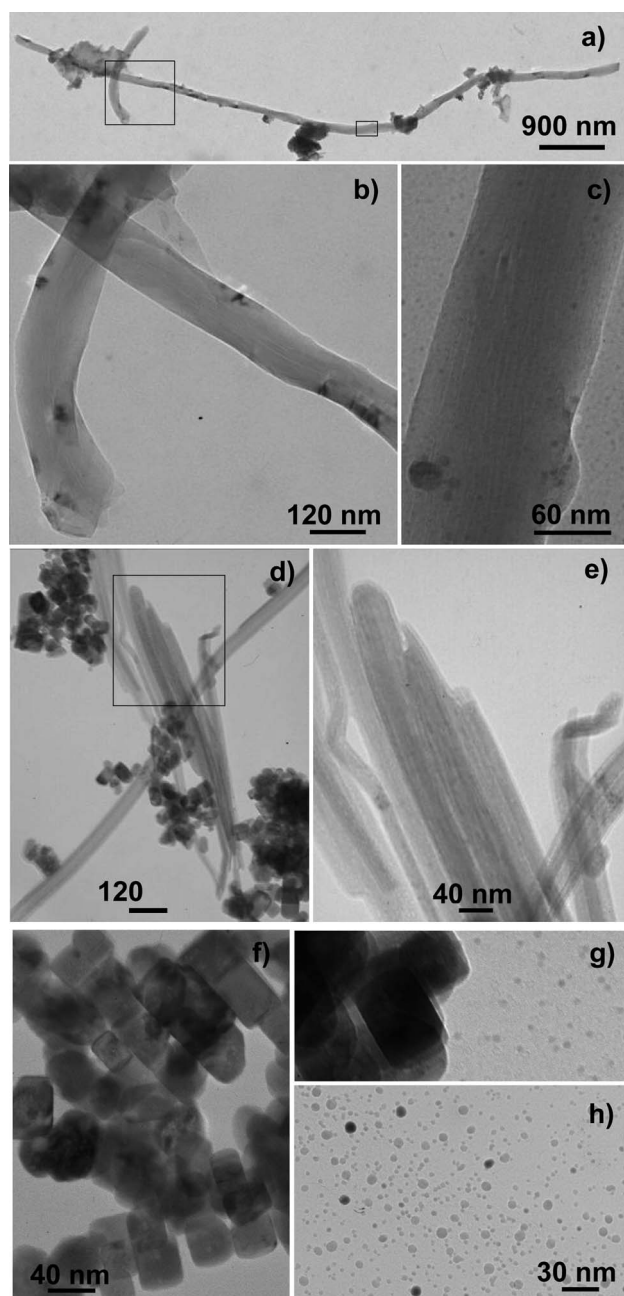


Fig. 5 TEM images of the mixed morphologies of HT $Gd_{1-x}Tm_xVO_4$ prepared at pH = 7: (a–c) long and flexible nanotubes (NTs) obtained after 13 h of HT synthesis; (d and e) alongside attached NTs after 13 h of HT synthesis; (f and g) nanoparticles (NPs) with square or rectangular sections after 24 h of HT synthesis; (h) nanodots coexisting with NPs in (f) and (g).

which are built of 10 edge-sharing $[VO_6]$ octahedra,⁴⁰ is the result of the nucleophilic condensation of the neutral molecular precursor $[VO(OH)_3(H_2O)_2]^0$ described for the pH range ~ 2 to 6 in the dispersion of hydrolyzed V^{5+} .^{17,41}



From bright orange dispersions solid decavanadate phases precipitate when cations are present. Several of such phases have

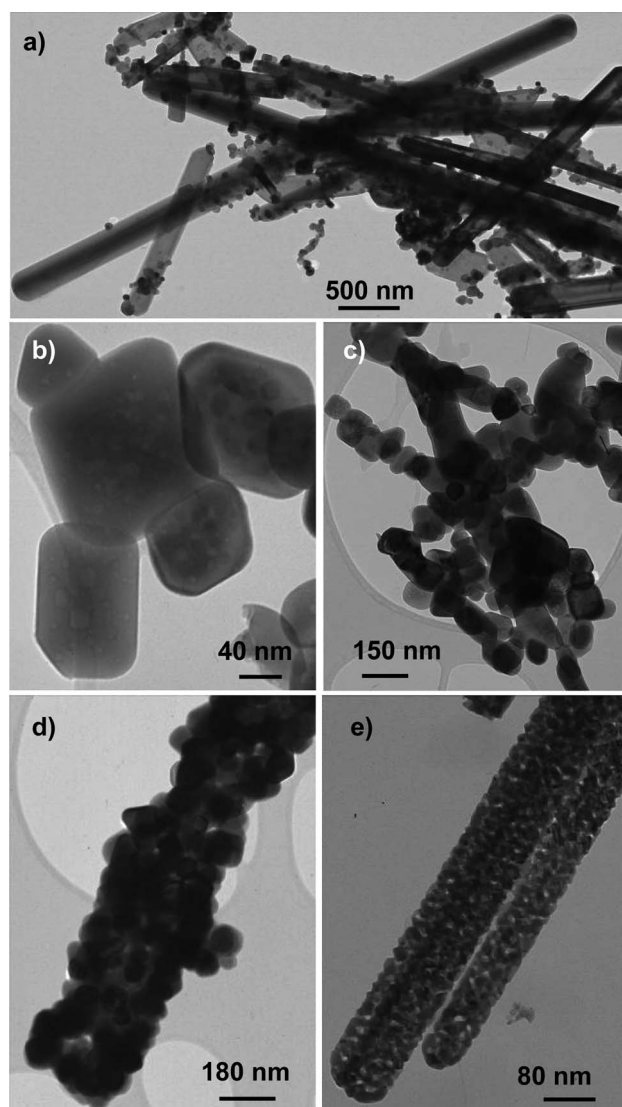


Fig. 6 TEM images of $Gd_{1-x}Tm_xVO_4$ after thermal annealing for 5 h at 600 °C of previous HT materials prepared in pH 4 media: (a) general overview showing nanobelts, nanorods and polygonal nanoparticles; (b) 3D nanoparticles with internal cavities; (c and d) aligned attachment of 3D nanoparticles; (e) porous nanorods.

been described with polyhedra of trivalent lanthanides situated among decavanadate clusters.^{42–47} Thus, it can be thought that in the starting dispersion these units act as precursors for the subsequent HT growth of 3D $Gd_{1-x}Tm_xVO_4$ NPs. The coalescence of these NPs for prolonged HT periods will be responsible of the growth of observed micrometre-size dense platelets as those shown in Fig. 4a–c. Furthermore, upon annealing the removal of water adsorbed in bubbles induces internal cavities in NPs, Fig. 6b, and their aggregation with a suitable crystallographic orientation, that is, by oriented attachment,⁴⁸ Fig. 6c and d, generates the observed nanorods, Fig. 6e. With the example of $Er_2V_{10}O_{28} \cdot 25(H_2O)$ (ref. 44) chosen owing to its VO_x parent structure of $[V_{10}O_{28}]^{6-}$ clusters, Fig. 9a–f schematically illustrate this condensation route for the formation of 3D NPs, platelets and large octahedral-like morphologies observed for HT $Gd_{1-x}Tm_xVO_4$ prepared in acidic pH.

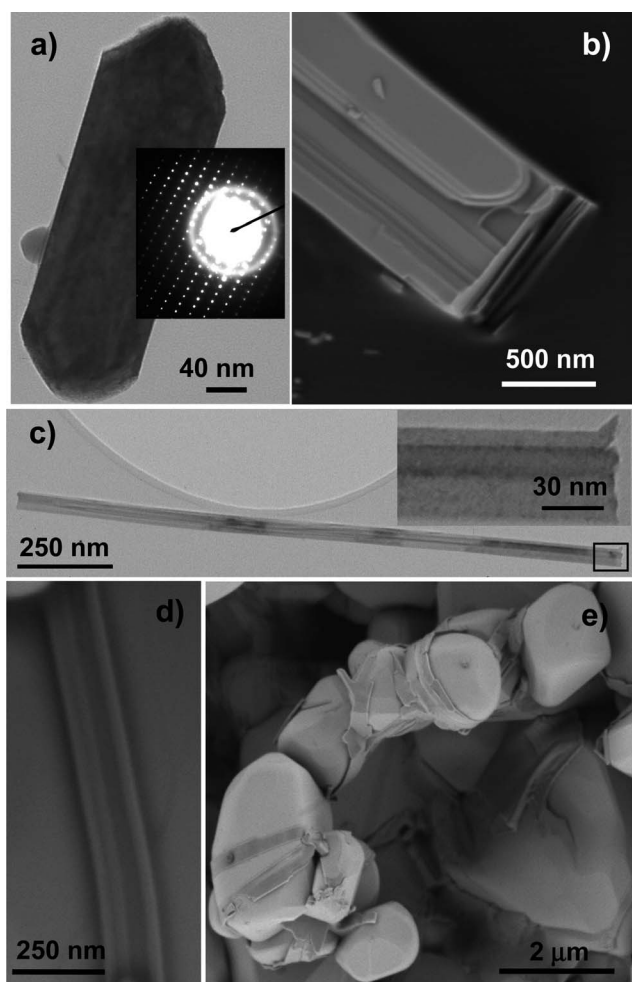


Fig. 7 Micrographs of pH 4–7 HT $Gd_{1-x}Tm_xVO_4$ after further thermal annealing for 5 h at 600 °C: (a) TEM image of a nanobelt (pH 4), the selected area electron diffraction (SAED) image shown in the inset confirms its high crystallinity; (b) FE-SEM image of dense stacked belts (pH 7); (c) TEM image of an individual rigid nanotube (pH 7); FE-SEM images of (d) assembled nanotubes (pH 7) and (e) agglomerated octahedral-like particles, which in some cases are encircled by nanobelts (pH 7).

Further investigations of the morphology of the observed polygonal forms by HRTEM support the above statements. HRTEM images of discrete NPs reveal in all cases a well-defined single crystal structure characteristic of the tetragonal $I4_1/amd$ symmetry of $GdVO_4$. From the lattice fringes in Fig. 10a, as well as the corresponding selected area electron diffraction (SAED) pattern in Fig. 10b, the resolved interplanar spacings are found to be about 0.359 nm, consistent with the d -spacing between (200) planes of $GdVO_4$ (JCPDS File 86-0996). The energy dispersive X-ray (EDX) spectrum for the particle in Fig. 10a is given in Fig. S5 in the ESI† section. Simulations of the crystal growth habit⁴⁹ for polygonal crystals indicate that their developed faces are typically {100}, {010} and {001}, Fig. 11a, and {101}, {011}, $\{10\bar{1}\}$ and $\{0\bar{1}1\}$, Fig. 11b; this observation indicates that despite being 3D crystals they have a well-developed plate-like character.⁵⁰

Moreover, the above molecular neutral precursor can be also involved in other condensation processes through nucleophilic addition of OH^- groups on positive V cations. The kinetically more favorable condensation (olation) pathway along the direction that includes the easily leaving H_2O molecule, Fig. 9a, produces chains of corner-sharing VO_5 pyramids, and then the slower condensation (oxolation) in the $HO-V-OH$ direction yields double chains of VO_5 units, Fig. 9g, which are linked by further oxolation involving the remaining OH group, Fig. 9h–l, and originate the ribbon and belt-like morphologies observed for $V_2O_5 \cdot nH_2O$ gels,^{41,51,52} where V_2O_5 layers are stabilized since the $V=O$ groups of edge-sharing pyramids lie on different sides of the plane. The current nanoribbon morphology displayed by annealed $Gd_{1-x}Tm_xVO_4$ samples prepared at pH 4, Fig. 7a and b, may have a parallel origin to that in $V_2O_5 \cdot nH_2O$ materials, that is, a highly anisotropic growth during the HT step explained by these successive condensation mechanisms from the precursor $[VO(OH)_3(H_2O)_2]^0$ in the initial hydrolyzed orange dispersion, which is finally stabilized by the subsequent thermal annealing. Additionally, the highly crystalline $Gd_{1-x}Tm_xVO_4$ nanoribbons self-stack in an ordered way giving rise to thicker ribbons. HRTEM analyses of our pH 4 HT annealed samples sustain the above path to the formation of nanoribbons. The high resolution image in Fig. 12a allows observation of prominent interplanar spacings of 0.472 nm, consistent with the d -spacing for (101) planes of $GdVO_4$, and the corresponding indexed SAED pattern can be seen in Fig. 12b. The EDX spectrum for the sample in Fig. 12a and b is given in Fig. S6 in the ESI† section. Images in Fig. 12a and b are fully reminiscent of those for “parent” orthorhombic V_2O_5 nanobelts, which for comparison are shown in Fig. S7a and b†, with the corresponding EDX spectrum in Fig. S7c†. The difference would lie in the evolution to a structural arrangement with VO_4^{3-} tetrahedra instead of that described with VO_5 pyramids. Thus, although the tetragonal $Gd_{1-x}Tm_xVO_4$ has not a truly layered structure, the V_2O_5 -related precursor induces a kind of pseudo-layered crystal growth habit in HT prepared samples. Among views of the $I4_1/amd$ zircon-type structure of $GdVO_4$ in Fig. S8a–d†, the latter Fig. S8d† underlines this aspect.

The formation of nanosheets as those depicted in Fig. 3c and d can be envisaged from the condensation of the anionic $[VO(OH)_4(H_2O)]^-$ species, which results by deprotonation of the above neutral precursor when the pH slightly increases. Main oxolation reactions along the four V–OH bond directions are now kinetically equivalent, thus leading to layered structures. Under current HT conditions separated layers can experience a rolling up process that yields tubular forms. The evidence of the rolling process for $Gd_{1-x}Tm_xVO_4$ NTs, Fig. 3g and h and 8a–e, from previous nanosheets is provided by the coexistence in the HT material of partially scrolled sheets and complete NTs. The process is illustrated in Fig. S9†, where the structure of $BaV_7O_{16} \cdot n(H_2O)$ is chosen to illustrate the layered structure resulting from the $[VO(OH)_4(H_2O)]^-$ condensation.⁵³

In the mechanism accounting for the conversion of layered precursors to tubular-like nanostructures the first step is the insertion of molecules or cationic species between the layers, which relax the interlayer interaction and are able to act as structure-directing templates. Subsequently, the HT treatment of lamellar composites generates NTs. Reported HT preparations

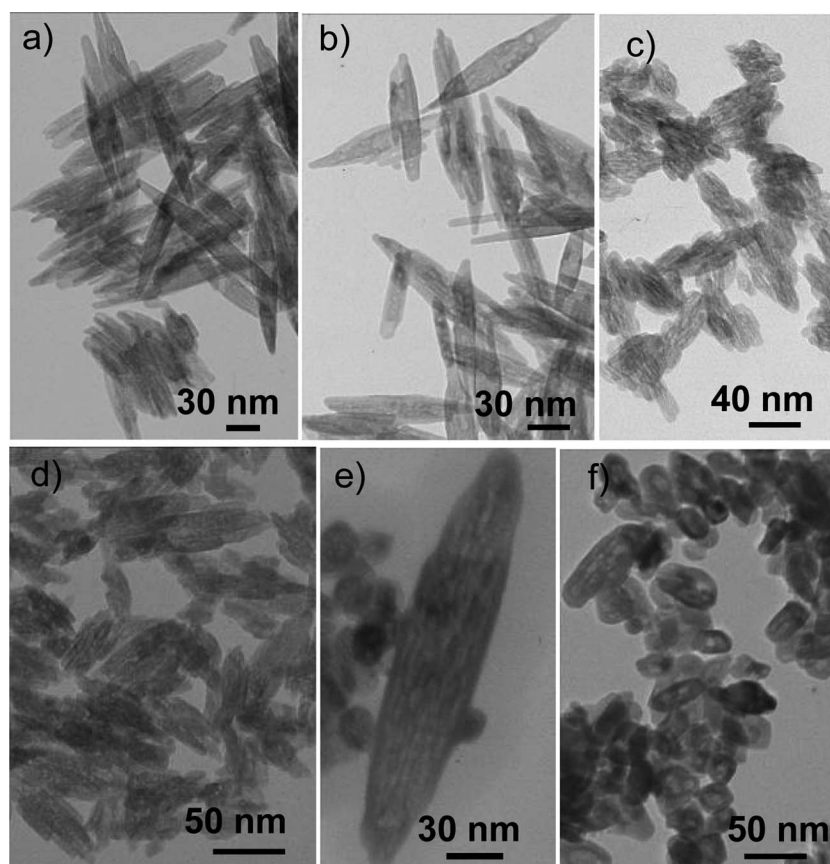


Fig. 8 TEM images of $Gd_{1-x}Tm_xVO_4$ prepared by HT treatment at pH 10: (a and b) spindle-like morphologies after 13 h of HT treatment of chloride reagents; (c and d) spindle-like forms after 6 h and 24 h of HT treatment of nitrates, respectively; (e) larger spindle after further annealing of $Gd_{1-x}Tm_xVO_4$ prepared by 2 days of HT treatment of nitrate reagents, with the dispersion previously aged for 3 days; (f) round-shaped grain morphology by annealing of $Gd_{1-x}Tm_xVO_4$ prepared by 6 h of HT treatment of nitrate reagents.

of multiwalled vanadium oxide nanotubes VO_x -NTs have been carried out by using a range of alkyl amines/diamines⁵⁴ and phenylamines⁵⁵ whose chain lengths determine both the distance between the walls of VO_x -NTs and its whole diameter.

Thus, following structural principles similar to those established to relate the flexible V_7O_{16} layers of $BaV_7O_{16} \cdot n(H_2O)$ to the generation of VO_x -NTs,⁵³ we can assume that the layered precursor compound in our orange/yellow material at pH ~ 4 to 7 has inserted or embedded Gd^{3+}/Tm^{3+} cations before the HT step, in a way that should be reminiscent of the final tetragonal zircon-type structure. The acid dissociation of surface-adsorbed hydroxyl groups $-V-OH + H_2O \rightarrow -V-O^- + H_3O^+$ will produce a large amount of free valences over the surface of the layer, and the attraction of Gd^{3+}/Tm^{3+} can satisfy these bonds to destabilize the planar forms. Thus, despite the absence of any kind of amines, the bend of these ‘composite layers’ prior to their HT induced scrolling can be related to the insertion/incorporation of trivalent Gd^{3+}/Tm^{3+} into the layered framework through an arrangement with vanadium building units being able to favor its curvature. Only $[V^{5+}O_4]$ tetrahedral units will constitute the walls in tubular $Gd_{1-x}Tm_xVO_4$, which represents another difference with VO_x -NTs, whose structure involves the simultaneous presence of square pyramids $[V^{5+}O_5]$ and tetrahedra $[V^{5+}O_4]$ in specific distributions.^{53,54,56,57} Furthermore, the reduction of V^{5+} to larger size V^{4+} does not seem to be an important contribution

to the scrolling of $Gd_{1-x}Tm_xVO_4$ nanosheets, as can be derived from unchanged color of final HT materials at pH ~ 4 to 7, that remain orange to pale yellow, and in fact only the material prepared under exhaustive ultrasonication after the HT step, shown in Fig. 3g and h, resulted to be greenish.

For pH above 7 the prepared dispersion prior to hydrothermal treatments contains $[H_nVO_4]^{(3-n)-}$ precursor species, which experiences a progressive deprotonation with the increase of pH. The molecular V^{5+} -precursors present in the pH range 8 to 10 are $[HVO_4]^{2-}$ and the completely deprotonated tetrahedral orthovanadate $[V^{5+}O_4]^{3-}$ units.^{17,41} Thus, only limited oxolation is possible with $[HVO_4]^{2-}$, which will yield ribbon-like structures constituted by $[VO_4]^{3-}$ tetrahedra, in a similar way to that described for V_2O_5 -related ribbons with chains of VO_5 pyramids. Current HT prepared $Gd_{1-x}Tm_xVO_4$ nanospindles, as in Fig. 8a–e, are formed afterwards by further auto-assembly of these nanoribbons. At the higher side of this pH range monomeric $[VO_4]^{3-}$ is the major species present, and since the absence of V–OH groups precludes further condensation and formation of V–O–V bonds and thus the existence of ribbon-like and layered structures, the HT treatment will produce only 3D $Gd_{1-x}Tm_xVO_4$ nanocrystals, as in Fig. 8f. The mixture of the spindle-like and round-shaped grain morphologies of $Gd_{1-x}Tm_xVO_4$ samples prepared by aging for 3 days the sol–gel dispersion prior to 2 days of HT treatment

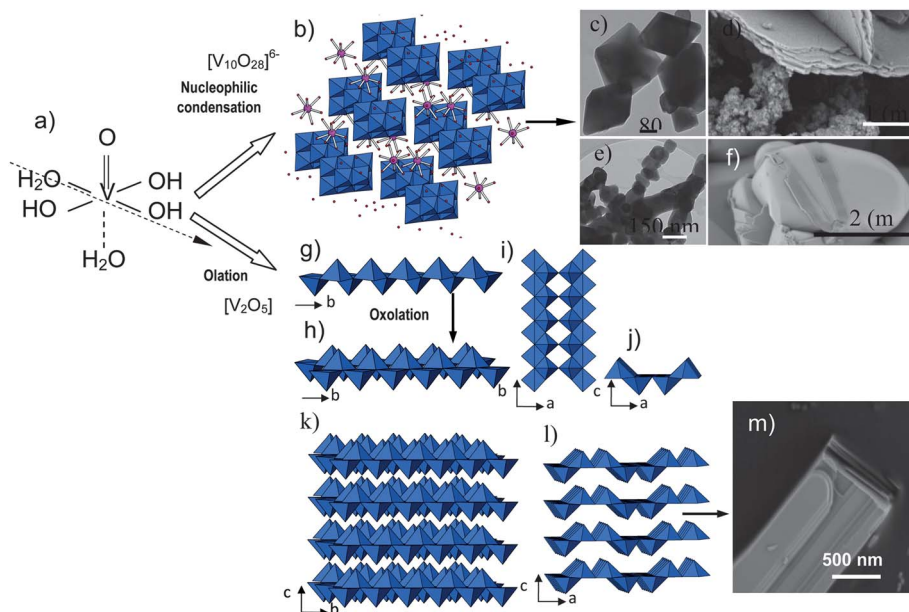


Fig. 9 Correlations between VO_x crystalline structures derived from the V^{5+} neutral molecular precursor $[\text{VO}(\text{OH})_3(\text{H}_2\text{O})_2]^0$ and morphologies of HT $\text{Gd}_{1-x}\text{Tm}_x\text{VO}_4$ prepared at acidic pH: (a) $[\text{VO}(\text{OH})_3(\text{H}_2\text{O})_2]^0$ precursor existent at acidic pH, the dot arrow indicates the direction of condensation; (b) nucleophilic condensation yielding 3D $[\text{V}_{10}\text{O}_{28}]^{6-}$ decavanadate clusters built of $[\text{VO}_6]$ octahedra, the structure corresponds to $\text{Er}_2\text{V}_{10}\text{O}_{28} \cdot 25(\text{H}_2\text{O})$,⁴⁴ with ErO_8 polyhedra among clusters; (c) 3D nanoparticles (NPs) of $\text{Gd}_{1-x}\text{Tm}_x\text{VO}_4$ prepared by 24 h HT treatment of the acid dispersion; (d) dense platelets of $\text{Gd}_{1-x}\text{Tm}_x\text{VO}_4$ formed by coalescence of NPs in (c) after 3 days of HT treatment; (e) alignment of $\text{Gd}_{1-x}\text{Tm}_x\text{VO}_4$ NPs in (c) after 5 h of thermal annealing at 600°C that finally yields nanorods; (f) dense micrometre size $\text{Gd}_{1-x}\text{Tm}_x\text{VO}_4$ particles also present after thermal annealing of NPs in (c); (g) double chains of $[\text{V}_2\text{O}_5]$ pyramids along the b direction formed by olation of $[\text{VO}(\text{OH})_3(\text{H}_2\text{O})_2]^0$; (h) ribbons of $[\text{V}_2\text{O}_5]$ pyramids after oxolation along b of the double chain in (g); (i and j) views in ab and ac planes, respectively, of the ribbon in (h); (k and l) views of c -stacked ribbons along a and b directions, respectively; (m) dense set of stacked ribbons or nanobelts.

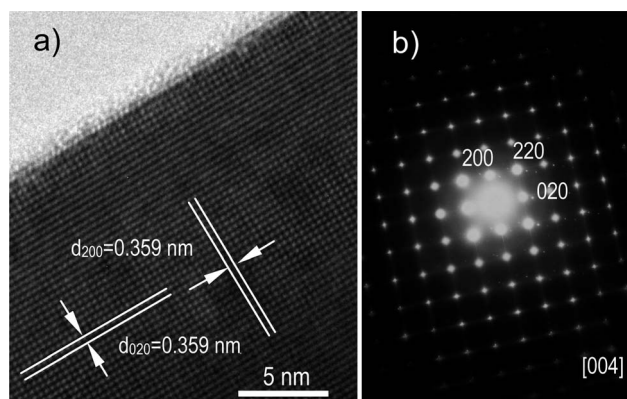


Fig. 10 (a) HRTEM image of a polygonal $\text{Gd}_{1-x}\text{Tm}_x\text{VO}_4$ nanoparticle prepared by 24 h hydrothermal treatment of the acid dispersion. (b) The corresponding SAED pattern along the $[004]$ zone axis.

could be due to the coexistence of both $[\text{HVO}_4]^{2-}$ and $[\text{VO}_4]^{3-}$ molecular species.

The developed general scheme of mechanisms for the formation of micro–nano morphologies for HT prepared $\text{Gd}_{1-x}\text{Tm}_x\text{VO}_4$ has been summarized in Fig. 13. For each set of synthesis conditions the aspects underlined by the current analysis are the critical role of the generated VO_x structure *versus* the secondary influence of $\text{Gd}^{3+}(\text{Tm}^{3+})\text{O}_8$ units on the final morphology of HT $\text{Gd}_{1-x}\text{Tm}_x\text{VO}_4$, and the amenability of such VO_x frameworks to the final pure zircon-type crystal structure.

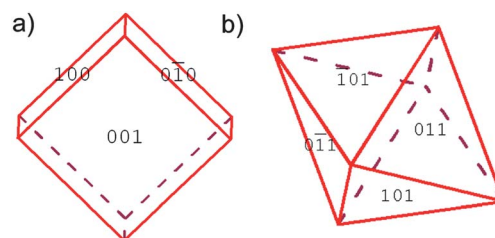


Fig. 11 Simulated shape of polygonal $\text{Gd}_{1-x}\text{Tm}_x\text{VO}_4$ nanoparticles prepared by 24 h HT treatment of the acid dispersion: (a) crystal habit with well developed faces $\{100\}$, $\{010\}$ and $\{001\}$ and (b) crystal habit with faces $\{101\}$, $\{011\}$, $\{101\}$ and $\{011\}$.

Assessment on room temperature spectroscopic properties

The current study has been focused in the photoluminescence (PL) of the ${}^3\text{H}_4$ and ${}^3\text{F}_4$ Tm^{3+} multiplets involved in the ${}^3\text{F}_4 \rightarrow {}^3\text{H}_6$ tunable laser emission at $1.80\text{--}2.05\ \mu\text{m}$,^{13,18,19} seen in the scheme that shows relevant pumping and de-excitations paths for this laser emission in Fig. S10†. Room temperature spectroscopic measurements have been performed on the series of $\text{Gd}_{1-x}\text{Tm}_x\text{VO}_4$ ($x = 0.002, 0.005, 0.01$ and 0.05) samples prepared using $\text{Gd}(\text{Tm})$ nitrates at pH 4, 7 and 10. The excitation spectrum of the ${}^3\text{H}_4$ multiplet as well as the infrared PL of ${}^3\text{H}_4 \rightarrow {}^3\text{F}_4$ ($\lambda_{\text{EMI}} = 1380\text{--}1550\ \text{nm}$) and ${}^3\text{F}_4 \rightarrow {}^3\text{H}_6$ ($\lambda_{\text{EMI}} = 1650\text{--}2000\ \text{nm}$) Tm^{3+} transitions were first monitored. Collected spectra are analogous for all tested samples, see Fig. S11† for a selected preparation, with transitions showing splittings similar

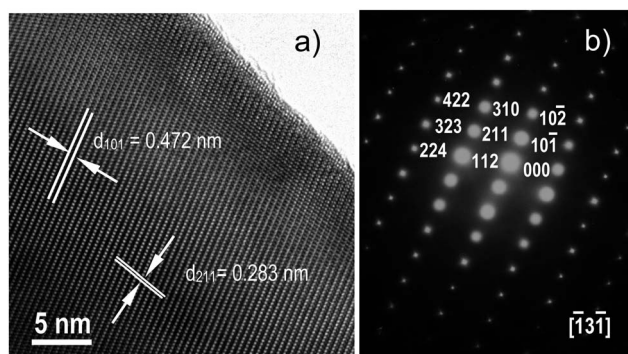


Fig. 12 (a) HRTEM image of a ribbon-like HT $\text{Gd}_{1-x}\text{Tm}_x\text{VO}_4$ prepared by HT treatment of the acid dispersion followed by annealing. (b) The corresponding SAED pattern along the $[\bar{1}31]$ zone axis.

to those reported for Tm^{3+} -doped GdVO_4 ¹⁸ and isostructural YVO_4 single crystals,^{20,21} which is an indication of the Tm^{3+} incorporation actually at the same crystal site than in single crystals.

Despite these similarities, possible modifications in dynamics of f-f Tm^{3+} luminescence transitions are expected with regards to bulk single crystals, particularly concerning nonradiative relaxation and energy transfer, associated with surface defects and interactions with phonon modes of surface adsorbed molecules resulting in the enhanced surface area due to the size reduction and porosity. From this point of view, different spectroscopic behaviors are envisaged between crude HT and further annealed samples, and also for each pH set of prepared samples. These differences can be confidently assessed through lifetime measurements.

The lifetime of the ${}^3\text{F}_4$ multiplet only can be experimentally tested through the relaxation to the ground ${}^3\text{H}_6$ multiplet, which is electronically populated. Consequently, the re-absorption of

the PL may lead to the sometimes observed artificial enlargement of its measured decay,^{13,18} which is more noticeable as the Tm^{3+} concentration increases. On the other hand a strong reduction of the lifetime is expected with the increase of the Tm^{3+} concentration, $[\text{Tm}^{3+}]$, and experimental values obtained in Tm^{3+} concentrated media usually do not represent the radiative lifetime of the ${}^3\text{F}_4$ multiplet. Thus, we have firstly analyzed the influence of the particle size and shape by using the ${}^3\text{H}_4 \rightarrow {}^3\text{F}_4$ transition, whose fluorescence is free of re-absorption.

A. ${}^3\text{H}_4$ lifetime in $\text{Gd}_{1-x}\text{Tm}_x\text{VO}_4$ ($0.002 \leq x \leq 0.05$) samples.

After short pulse excitation at $\lambda_{\text{EXC}} = 800$ nm the ${}^3\text{H}_4$ PL intensity decay of $\text{Gd}_{1-x}\text{Tm}_x\text{VO}_4$ samples was measured at the maximum of the ${}^3\text{H}_4 \rightarrow {}^3\text{F}_4$ emission range, $\lambda_{\text{EMI}} = 1470$ nm (see Fig. S11†). Crude HT samples prepared at pH 7 were initially analyzed. Their ${}^3\text{H}_4$ PL decays are always non-exponential, and the corresponding measured lifetimes τ are shorter than those in bulk crystals, 52 μs for 2 at% Tm in GdVO_4 ,¹⁸ 176 μs (ref. 18) and 130 μs (ref. 21) for 0.5 at% Tm in isostructural YVO_4 . Values of τ increase for longer HT syntheses and for lower Tm^{3+} doping levels, evolving from a few μs to 117 μs for $\text{Gd}_{0.998}\text{Tm}_{0.002}\text{VO}_4$ synthesized for $t = 2\frac{1}{2}$ h to 24 h. This reduction in the measured ${}^3\text{H}_4$ lifetime may be partially related to the contamination with hydrous species in the considerably larger surface of NPs, which is a usual rule in all low temperature routes of synthesis. To test this possibility we continued measuring the ${}^3\text{H}_4$ PL decays with all the samples annealed for 5 h at 600 °C, in which this contamination has been mostly removed.

Longer fluorescence τ values were obtained for annealed samples, see a comparative example in Fig. 14a, and depending on their pH origin ${}^3\text{H}_4$ PL decays behave differently. For pH 4-prepared samples single exponential decays are observed typically below $x = 0.01$ (1 at% Tm), independent of the HT treatment time, and only the highest concentrated sample $x = 0.05$ (5 at% Tm) shows in all cases a non-single exponential regime,

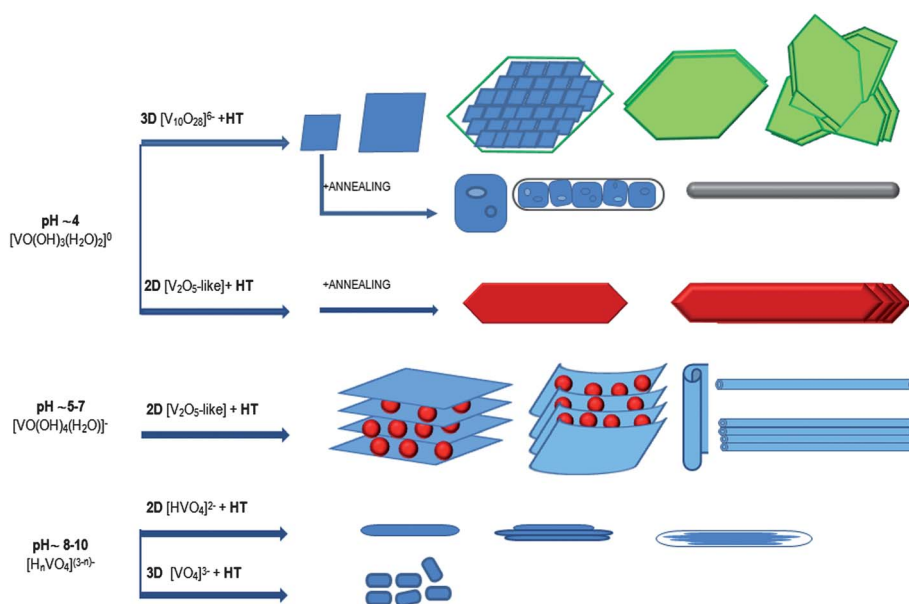


Fig. 13 Scheme of proposed mechanisms for the formation of HT and annealed $\text{Gd}_{1-x}\text{Tm}_x\text{VO}_4$ micro- and nanostructures depending on the pH of the solution medium.

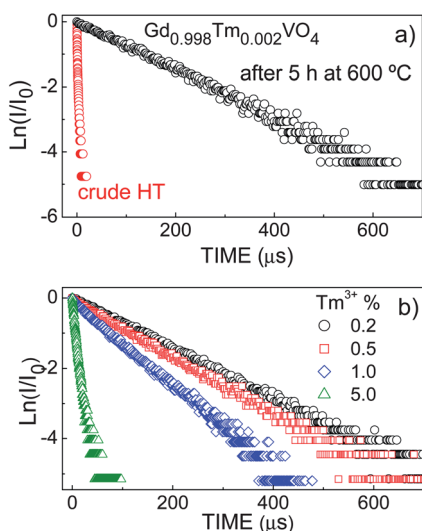


Fig. 14 300 K photoluminescence intensity decay of the ${}^3\text{H}_4$ multiplet of Tm^{3+} in $\text{Gd}_{1-x}\text{Tm}_x\text{VO}_4$ nanocrystals: (a) comparison of behaviors for crude HT (pH 7, $t = 2\frac{1}{2}$ h) and annealed $x = 0.002$ (0.2 at% Tm^{3+}) samples and (b) for different x contents prepared by 24 h HT synthesis at pH 4 with further annealing at $600\text{ }^\circ\text{C}$. $\lambda_{\text{EXC}} = 800\text{ nm}$ and $\lambda_{\text{EMI}} = 1470\text{ nm}$. Measurements were carried out on samples supported in ethylene glycol.

see Fig. 14b for samples prepared after 24 h of HT treatment. ${}^3\text{H}_4$ decays for pH 7 and 10 samples display in general a non-single exponential regime along the whole prepared $[\text{Tm}^{3+}]$ range, even for the most diluted sample $x = 0.002$ (0.2 at% Tm). Therefore, pH 4-prepared samples show time dependences of the ${}^3\text{H}_4$ PL intensity that can be correlated to that observed in single crystals for low enough and intermediate $[\text{Tm}^{3+}]$ levels, that is, an exponential decay followed by a more complex relationship, the latter is due to the resonant transfer between ${}^3\text{H}_4$ multiplets and ${}^3\text{H}_4 \rightarrow {}^3\text{F}_4$ cross-relaxation as the main Tm–Tm interactions. On the other hand, ${}^3\text{H}_4$ decays for pH 7 and 10 samples do not behave as usual in single crystals,⁵⁸ that is, independent of both pH and HT treatment time, in no case the single exponential decay is recovered for the higher concentrated sample, which indicates the small contribution of fast diffusion between excited ${}^3\text{H}_4$ multiplets as a nonradiative energy migration mechanism for the prepared 5 at% Tm- GdVO_4 samples. Anyway, taking into account the usual closeness between Tm^{3+} concentrations yielding diverse decay regimes, we have analyzed the ${}^3\text{H}_4$ PL decays of $\text{Gd}_{1-x}\text{Tm}_x\text{VO}_4$ samples considering a double exponential model. The fast component at short times (I_1 , τ_1) would correspond to the emission of Tm^{3+} ions at the surface of nanocrystals, and the longest one (I_2 , τ_2) to Tm^{3+} ions within the body of nanocrystals, the latter in principle should approach the lifetime value obtained in Tm-doped GdVO_4 single crystals, since the crystal field for Tm^{3+} centers would be unperturbed. In order to obtain significant results the long-lived lifetime was first calculated from the tail of the $\ln(I/I_0)$ vs. time plots, and later we fitted the intensity decay, $I(t)$, to a curve $I(t) = I_1 e^{-t/\tau_1} + I_2 e^{-t/\tau_2}$, with $I_1 + I_2 = 1$. The procedure has systematically produced good fits of our experimental ${}^3\text{H}_4$ PL decays, and complete results are shown in Table S1†. It can be seen that the time of the HT treatment does not affect significantly the long-lived ${}^3\text{H}_4$ τ_2 value

for a given pH and Tm^{3+} content. The value of ${}^3\text{H}_4$ τ_2 increases for lower Tm^{3+} concentrations, varying from 10–46 μs (5 at% Tm^{3+}) up to 126–155 μs (0.2 at% Tm^{3+}), this latter value being close to $\tau_{\text{RAD}} = 174\text{ }\mu\text{s}$.¹⁸ Fig. 15a–c depict an overview of the evolution of τ_2 with $[\text{Tm}^{3+}]$ for the three sets of samples prepared with pH 4, 7 and 10. For $\text{Gd}_{1-x}\text{Tm}_x\text{VO}_4$ samples of the two latter groups the component I_1 of the double exponential decay experiences an enhancement with the Tm^{3+} concentration reaching values of $I_1 = 0.60$ – 0.85 for 5 at% Tm^{3+} .

B. ${}^3\text{F}_4$ lifetime in $\text{Gd}_{1-x}\text{Tm}_x\text{VO}_4$ ($0.002 \leq x \leq 0.05$) samples.

After short pulse excitation at $\lambda_{\text{EXC}} = 800\text{ nm}$ the signal of ${}^3\text{F}_4$ PL decay for crude HT samples was below our detection level. However, after thermal annealing of samples these decays were satisfactorily measured at the maximum of the ${}^3\text{H}_4 \rightarrow {}^3\text{H}_6$ emission range, $\lambda_{\text{EMI}} = 1816\text{ nm}$ (see Fig. S11†). F_4 decays are more often single exponential than for ${}^3\text{H}_4$, and this trend is favored by lower $[\text{Tm}^{3+}]$ in the sample, the acidic pH and the prolonged HT treatment, that is, while for pH 4 almost all samples show single exponential ${}^3\text{F}_4$ PL decay independent of the HT time, at pH 10 only samples HT prepared for 24 h display single exponential decays. A double exponential analysis has been applied in the same way that previously indicated for the ${}^3\text{H}_4$ multiplet, see the results in Table S2†. Examples of ${}^3\text{F}_4$ PL intensity decays for $\text{Gd}_{1-x}\text{Tm}_x\text{VO}_4$ samples from different preparative conditions are shown in Fig. 16a–f, and the overview of the evolution of measured lifetimes τ (or long-lived τ) with $[\text{Tm}^{3+}]$ for the three sets of samples with pH 4, 7 and 10 appears in Fig. 17a–c.

Measured τ values are getting higher in the sequence $\tau_{\text{pH}10} < \tau_{\text{pH}4} < \tau_{\text{pH}7}$. For the lowest concentrated samples, 0.2 at% Tm^{3+} , fluorescence lifetimes are typically within the range $\tau = 600$ to $900\text{ }\mu\text{s}$, with the higher values corresponding to samples prepared at pH 7, for which even a $990\text{ }\mu\text{s}$ lifetime has been measured, Fig. 16f.

Thus, ${}^3\text{F}_4$ fluorescence lifetimes for pH 7-samples are very close to the calculated radiative lifetime $\tau_{\text{RAD}} = 1036\text{ }\mu\text{s}$ for Tm^{3+} in GdVO_4 crystal, and moreover they are likely free of lengthening by re-absorption-related effects that seem largely affecting measurements in GdVO_4 or YVO_4 single crystals.^{18,22} Superior τ values for pH 7-samples with regards to pH 4 ones should be correlated rather with the aggregation of primary nanoparticles into micro-sized structures, which are larger in the former, than

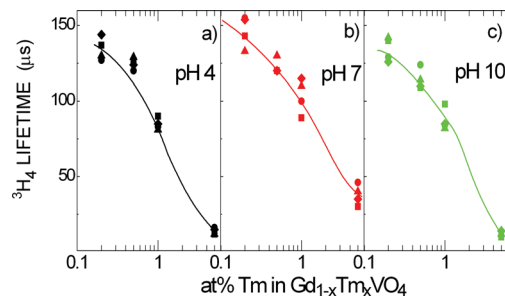


Fig. 15 Dependence on the Tm^{3+} content of the 300 K long-lived ${}^3\text{H}_4$ lifetime in $\text{Gd}_{1-x}\text{Tm}_x\text{VO}_4$ prepared by HT treatment ($t = 2\frac{1}{2}$ h ■, 6 h ●, 13 h ▲, 24 h ◆) and further $600\text{ }^\circ\text{C}$ thermal annealing: (a) pH 4, (b) pH 7 and (c) pH 10. $\lambda_{\text{EXC}} = 800\text{ nm}$ and $\lambda_{\text{EMI}} = 1470\text{ nm}$.

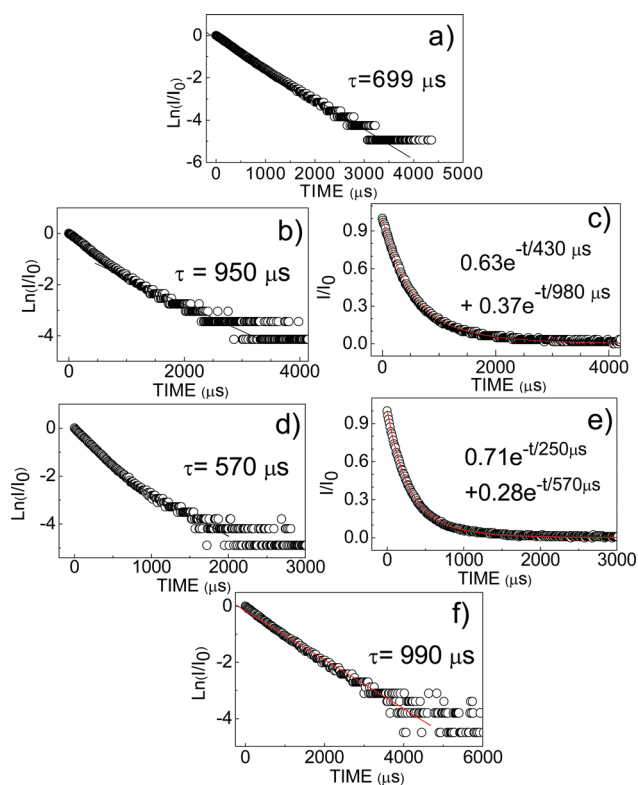


Fig. 16 Comparison of 300 K PL intensity decays of the 3F_4 multiplet of Tm^{3+} in $Gd_{0.995}Tm_{0.005}VO_4$ nanocrystals prepared by 2.5 h HT treatment at different pHs followed by annealing of 5 h at 600 °C: (a) pH 4; (b) and (c) pH 7; (d) and (e) pH 10. (f) 300 K 3F_4 PL decay of $Gd_{0.998}Tm_{0.002}VO_4$ annealed after 6 h of HT treatment at pH 7. The points are the experimental results, and the continuous lines are the fits: (a and f) the single exponential fits; (b and d) the linear fit of the tail of the plot; (c and e) the fit with two exponential decays, as indicated in each case. $\lambda_{EXC} = 800$ nm and $\lambda_{EMI} = 1816$ nm.

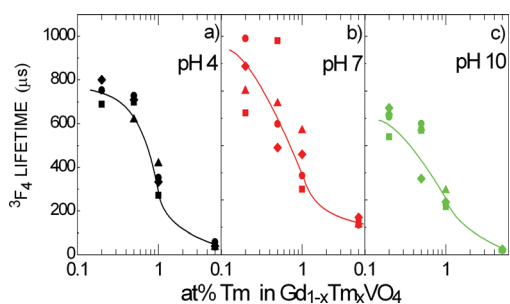


Fig. 17 Dependence on the Tm^{3+} content of the 300 K long-lived 3F_4 lifetime in $Gd_{1-x}Tm_xVO_4$ prepared by HT treatment ($t = 2\frac{1}{2}$ h ■, 6 h ●, 13 h ▲, 24 h ◆) at (a) pH 4, (b) pH 7 and (c) pH 10, followed by 5 h thermal annealing at 600 °C. $\lambda_{EXC} = 800$ nm and $\lambda_{EMI} = 1816$ nm.

with the corresponding specific surfaces S_{BET} , that being considerably lower for pH 4-samples would support fewer defects and adsorbed species capable of causing effective quenching of the luminescence of the excited 3F_4 multiplet through nonradiative relaxation processes. On the other hand, well dispersed homogeneous nanospindle-like samples prepared at pH 10, despite having the highest specific surfaces associated

with their nanosize and porosity, still retain considerable emission efficiency when compared to single crystals.

The measured 3F_4 lifetime progressively shortens with the increase of the Tm^{3+} concentration, and for 5 at% Tm^{3+} -doped samples achieved values are visibly different, following the already indicated trend in the function of the pH, $\tau = 20\text{--}25$ μs , 35–60 μs and 135–170 μs for pH 10, 4 and 7, respectively, see Table S2†. In Tm^{3+} concentrated samples the largest source of nonradiative processes is fast diffusion, through which 3F_4 decays recover a single exponential behavior in single crystals. Comparing the three sets of 5 at% Tm^{3+} pH-derived prepared samples, only pH 7 materials continue to show two decay regimes for the 3F_4 fluorescence, with Tm^{3+} active centers at the core of the particle showing substantially higher measured lifetimes. Thus fast diffusion seems to be less favored in pH 7 samples up to the tested 5 at% Tm^{3+} doping level; this may be due to the presence of nanoparticle frontiers within the aggregates leading to a recovery time.

4. Conclusions

Chemical processes involving low temperature HT treatments of pH 4, 7 and 10 solutions of Gd(Tm)-nitrates or chloride reagents and NH_4VO_3 result in the formation of crystalline nanorods, nanotubes, nanoribbons, nanospindles or 3D micro- and nanoparticles of Tm-doped zircon-type $GdVO_4$. Each of these morphologies depends critically on the structural arrangement generated by specific V^{5+} -molecular precursors as well as the HT conditions, in such a way that in the absence of capping agents nearly homogeneous size distribution of a single morphology—porous nanospindles—can be prepared only at 10 or higher pH. Average sizes of crystalline primary nanoparticles are smaller for samples prepared at higher pH, and S_{BET} values concomitantly increase, however bulky aggregates of these nanoparticles are found for Tm- $GdVO_4$ prepared at pH 7.

The prepared micro- and nanosized Tm- $GdVO_4$ samples show excitation and photoluminescence spectra of 3H_4 and 3F_4 Tm^{3+} multiplets involved in the ~ 2 μm laser emission equivalent to those in single crystals, *i.e.*, with very similar band shapes and energies of optical transitions. Room temperature measurements of the luminescence decay of these excited states show mostly nonexponential dynamics for 3H_4 , whereas the analysis of 3F_4 in further annealed samples indicates a trend for single exponential decays in lower Tm^{3+} concentrated samples, especially those prepared by prolonged HT treatment in acid media, and a two-regime decay for higher Tm^{3+} concentrated samples, which becomes noticeable for materials prepared in neutral to basic media. These luminescence decays have been analytically well reproduced by the sum of two exponential regimes ascribed to different rates for nonradiative relaxations in defects at the surface and in the core of particles. 3H_4 and 3F_4 fluorescence lifetimes evolve in the sequence $\tau_{pH10} < \tau_{pH4} < \tau_{pH7}$, and higher values of $\tau = 155$ μs and $\tau = 990$ μs for lower concentrated 0.2 at% Tm^{3+} materials are close to the radiative lifetimes for Tm^{3+} in the $GdVO_4$ crystal, $\tau_{RAD} = 174$ and $\tau_{RAD} = 1036$ μs , respectively. Preserved fluorescence lifetimes and thus emission efficiencies in pH 7 samples correlate with the presence of large aggregates of primary nanoparticles, that is, with bulkier morphologies more close to a single crystal.

Acknowledgements

This work was supported by the Spanish Ministry of Science and Innovation under projects MAT2008-06729-C02-01 and MAT2011-29255-C02-01. RCV acknowledges her fellowship BES 2009-021748.

References

- 1 J. W. Stouwdam and F. C. J. M. van Veggel, *Langmuir*, 2004, **20**, 11763.
- 2 J. W. Stouwdam and F. C. J. M. van Veggel, *Nano Lett.*, 2002, **7**, 733.
- 3 F. Esteban-Betegón, C. Zaldo and C. Cascales, *Chem. Mater.*, 2010, **22**, 2315.
- 4 F. Esteban-Betegón, C. Zaldo and C. Cascales, *Inorg. Chem.*, 2011, **50**, 2836–2843.
- 5 E. W. Barrera, M. C. Pujol, F. Díaz, S. B. Choi, F. Rotermund, K. H. Park, M. S. Jeong and C. Cascales, *Nanotechnology*, 2011, **22**, 075205.
- 6 F. Vetrone, J. C. Boyer, J. A. Capobianco, A. Speghini and M. Bettinelli, *J. Phys. Chem. B*, 2003, **107**, 1107.
- 7 W. Kim, M. Nyk and P. Prasad, *Nanotechnology*, 2009, **20**, 185301.
- 8 J. Shen, L.-D. Sun, J.-D. Zhu, L.-H. Wei, H.-F. Sun and C.-H. Yan, *Adv. Funct. Mater.*, 2010, **20**, 3708.
- 9 K. Binnemans, *Chem. Rev.*, 2009, **109**, 4283.
- 10 M. Tokurakawa, K. Takaichi, A. Shirakawa, K. Ueda, H. Yagi, S. Hosokawa, T. Yanagitani and A. A. Kaminskii, *Opt. Express*, 2006, **14**, 12832.
- 11 C. Pan, D. Zhang and L. Shi, *J. Solid State Chem.*, 2008, **181**, 1298.
- 12 D. Zhang, F. Niu, T. Yan, L. Shi, X. Du and J. Fang, *Appl. Surf. Sci.*, 2011, **257**, 10161.
- 13 A. I. Zagumennyi, V. A. Mikhailov, V. I. Vlasov, A. A. Sirotkin, V. I. Podreshetnikov, Y. L. Kalachev, Y. D. Zavartsev, S. A. Kutovoi and I. A. Shcherbakov, *Laser Phys.*, 2003, **13**, 311.
- 14 K. Scholle, S. Lamrini, P. Koopmann and P. Fuhrberg, 2 μm Laser Sources and Their Possible Applications, in *Frontiers in Guided Wave Optics and Optoelectronics*, ed. B. Pal, INTECH, Croatia, 2010, pp. 471–499, ISBN 978-953-7619-82-4.
- 15 P. Černý and H. Jelínková, *Developing Thulium Lasers for Depth-Selective Scalpels*, SPIE, 2006, DOI: 10.1117/2.1200607.0281.
- 16 A. A. Lagatsky, X. Han, M. D. Serrano, C. Cascales, C. Zaldo, S. Calvez, M. D. Dawson, J. A. Gupta, C. T. A. Brown and W. Sibbett, *Opt. Lett.*, 2010, **35**, 3027.
- 17 J. Livage, *Materials*, 2010, **3**, 4175.
- 18 R. Lisiecki, P. Solarz, G. Dominiak-Dzik, W. Ryba-Romanowski, M. Sobczyk, P. Cerný, J. Šulc, H. Jelínková, Y. Urata and M. Higuchi, *Phys. Rev. B: Condens. Matter Mater. Phys.*, 2006, **74**, 035103.
- 19 M. J. D. Esser, D. Preussler, E. H. Bernhardt, C. Bolling and M. Posewang, *Appl. Phys. B: Lasers Opt.*, 2009, **97**, 351.
- 20 R. Lisiecki, B. Macalik, G. Dominiak-Dzik, P. Solarz, B. Nowak, W. Ryba-Romanowski, J. K. Jabczynski and T. Lukaszewicz, *Appl. Phys. B: Lasers Opt.*, 2008, **90**, 477.
- 21 F. S. Ermeneux, C. Goutaudier, R. Moncorgé, M. T. Cohen-Adad, M. Bettinelli and E. Cavalli, *Opt. Mater.*, 1997, **8**, 83.
- 22 M. Higuchi, K. Kodaira, Y. Urata, S. Wada and H. Machida, *J. Cryst. Growth*, 2004, **265**, 487.
- 23 E. W. Barrera, M. C. Pujol, C. Cascales, C. Zaldo, K. H. Park, S. B. Choi, F. Rotermund, J. J. Carvajal, X. Mateos, M. Aguiló and F. Díaz, *Appl. Phys. B: Lasers Opt.*, 2012, **106**, 409.
- 24 T. Yao, Y. Oka and N. Yamamoto, *Mater. Res. Bull.*, 1992, **27**, 669.
- 25 S. D. Huang and Y. Shan, *Chem. Commun.*, 1998, 1069.
- 26 T. Roisnel and J. Rodriguez-Carvajal, WinPLOTR, <http://www-llb.ccea.fr/fullweb/winplotr/winplotr.htm>.
- 27 C. J. Szepesi and J. H. Adair, *J. Am. Ceram. Soc.*, 2011, 1–8.
- 28 K. Nakamoto, *Infrared and Raman Spectra of Inorganic and Coordination Compounds*, John Wiley&Sons, New York, 1986.
- 29 J. W. Stouwdam, M. Raudsepp and F. C. J. M. van Veggel, *Langmuir*, 2005, **21**, 7003.
- 30 C. Yu, M. Yu, C. Li, C. Zhang, P. Yang and J. Lin, *Cryst. Growth Des.*, 2009, **9**, 785.
- 31 R. K. Selvan, A. Gedanken, P. Anilkumar, G. Manikandan and C. Karunakaran, *J. Cluster Sci.*, 2009, **20**, 291.
- 32 H. Wu, H. Xu, Q. Su, T. Chen and M. Wu, *J. Mater. Chem.*, 2003, **13**, 1223.
- 33 W. Fu, W. Zhao, L. You, X. Song, W. Zhang, H. Yu and S. Sun, *J. Solid State Chem.*, 2004, **177**, 4399.
- 34 Y. Wang, Y. Zuo and H. Gao, *Mater. Res. Bull.*, 2006, **41**, 2147.
- 35 J. Liu and Y. Li, *J. Mater. Chem.*, 2007, **17**, 1797.
- 36 B. Yan and J.-F. Gu, *J. Exp. Nanosci.*, 2009, **4**, 301.
- 37 Y. Zheng, H. You, G. Gia, K. Liu, Y. Song, M. Yang and H. Zhang, *Cryst. Growth Des.*, 2009, **9**, 5101.
- 38 L. Qian, J. Zhu, Z. Chen, Y. Gui, Q. Gong, Y. Yuan, J. Zai and X. Qian, *Chem.–Eur. J.*, 2009, **15**, 1233.
- 39 F. He, P. Yang, N. Niu, W. Wang, S. Gai, D. Wang and J. Lin, *J. Colloid Interface Sci.*, 2010, **343**, 71.
- 40 H. T. Evans, *Inorg. Chem.*, 1966, **5**, 967.
- 41 J. Livage, *Chem. Mater.*, 1991, **3**, 578.
- 42 Yu. N. Saʼfyanov and N. V. Belov, *Dokl. Akad. Nauk SSSR*, 1976, **227**, 1112.
- 43 Yu. N. Saʼfyanov, E. A. Kuz'min and N. V. Belov, *Dokl. Akad. Nauk SSSR*, 1978, **242**, 603.
- 44 B. E. Rivero, G. Rigotti, G. Punte and A. Navaza, *Acta Crystallogr., Sect. C: Cryst. Struct. Commun.*, 1984, **40**, 715.
- 45 B. E. Rivero, G. Punte and G. Rigotti, *Acta Crystallogr., Sect. C: Cryst. Struct. Commun.*, 1985, **41**, 817.
- 46 H. Naruke, T. Yamase and M. Kaneko, *Bull. Chem. Soc. Jpn.*, 1999, **72**, 1175.
- 47 X. H. Peng, Y. Z. Li, L. X. Cai, L. F. Wang and J. G. Wu, *Acta Crystallogr., Sect. E: Struct. Rep. Online*, 2002, **58**, i111.
- 48 R. L. Penn and J. F. Banfield, *Science*, 1998, **281**, 969.
- 49 E. Dowty, *SHAPE for Windows, Software for Drawing Crystal Shapes*, v.7.2.1, 2006.
- 50 K. Byrappa, C. K. Chandrashekar, B. Basavalingu, K. M. LokanathaRay, S. Ananda and M. Yoshimura, *J. Cryst. Growth*, 2007, **306**, 94.
- 51 M. Giorgetti, S. Passerini and W. H. Smyrl, *Inorg. Chem.*, 2000, **39**, 1514.
- 52 B. Li, Y. Xu, G. Rong, M. Jing and Y. Xie, *Nanotechnology*, 2006, **17**, 2560.
- 53 M. Wörle, F. Krumeich, F. Bieri, H.-J. Muhr and R. Nesper, *Z. Anorg. Allg. Chem.*, 2002, **628**, 2778.
- 54 F. Krumeich, H.-J. Muhr, M. Niederberger, F. Bieri, B. Schnyder and R. Nesper, *J. Am. Chem. Soc.*, 1999, **121**, 8324.
- 55 F. Sediri, F. Touati and N. Gharbi, *Mater. Lett.*, 2007, **61**, 1946.
- 56 V. Petkov, P. Y. Zavalij, S. Lutta, M. S. Whittingham, V. Parvanov and S. Shastri, *Phys. Rev. B: Condens. Matter Mater. Phys.*, 2004, **69**, 9085410.
- 57 F. Krumeich, H.-J. Muhr, M. Niederberger, F. Bieri and R. Nesper, *Z. Anorg. Allg. Chem.*, 2000, **626**, 2208.
- 58 J. M. Cano-Torres, M. Rico, X. Han, M. D. Serrano, C. Cascales, C. Zaldo, V. Petrov, U. Griebner, X. Mateos, P. Koopmann and C. Kränkel, *Phys. Rev. B: Condens. Matter Mater. Phys.*, 2011, **84**, 174207.